Journal of Power Sources 401 (2018) 303–311

Contents lists available at ScienceDirect

Journal of Power Sources

journal homepage: www.elsevier.com/locate/jpowsour

Improvement in the performance of inverted planar perovskite solar cells via the $CH_3NH_3PbI_{3-x}Cl_x$:ZnO bulk heterojunction

Zhiyong Liu[a,*], Tingwei He[a,b], Huihui Wang[c], Sagar M. Jain[d,**], Kaikai Liu[a], Jien Yang[a,b], Na Zhang[a], Hairui Liu[a], Mingjian Yuan[b,***]

[a] Henan Key Laboratory of Photovoltaic Materials, Department of Physics and Materials Science, Henan Normal University, Xinxiang, 453007, China
[b] Department of Chemistry, Nankai University, Tianjin, 300071, China
[c] College of Civil Engineering and Architecture, Jiaxing University, Zhejiang, 314001, China
[d] SPECIFIC, College of Engineering, Swansea University Bay Campus, Fabian Way, SA1 8EN, Swansea, United Kingdom

HIGHLIGHTS

- A $CH_3NH_3PbI_{3-x}Cl_x$:ZnO bulk heterojunction exits in the perovskite solar cell.
- ZnO nanoparticles improve light harvesting efficiency of perovskite solar cell.
- ZnO nanoparticles lead to the formation of large-size perovskite crystals.
- ZnO nanoparticles improve conductivity and electron mobility of perovskite film.

GRAPHICAL ABSTRACT

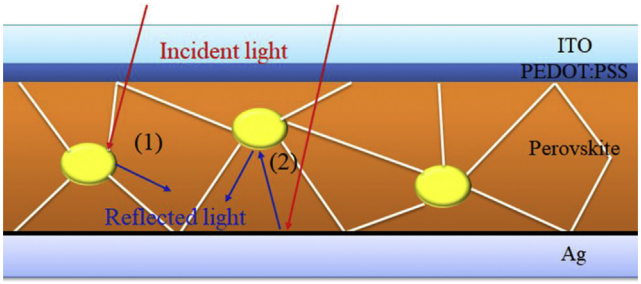

ARTICLE INFO

Keywords:
Perovskite solar cell
Zinc oxide
Bulk heterojunction
Absorption
Electron mobility

ABSTRACT

Zinc oxide (ZnO) as an electron transport material has been used in regular planar perovskite solar cells (PSCs). Herein, ZnO nanoparticles serve as an additive directly in perovskite active layer in order to fabricate a bulk-heterojunction inverted planar PSC. The $CH_3NH_3PbI_{3-x}Cl_x$:ZnO bulk heterojunction is prepared by mixing ZnO nanoparticles into $CH_3NH_3PbI_{3-x}Cl_x$ precursor solution. ZnO nanoparticles act as catalytic centers and induce the growth of perovskite grains leading to the formation of large-size perovskite crystals. Remarkably, hysterysis-free power conversion efficiency of 17.26% is achieved when precisely control the concentration of ZnO nanoparticles in $CH_3NH_3PbI_xCl_{3-x}$:ZnO bulk heterojunction active layer. The presence of ZnO nanoparticles in the perovskite films enhances the conductivity and electron mobility. Efficient charge injection of $CH_3NH_3PbI_xCl_{3-x}$:ZnO film can improve charge extraction in the PSCs. Moreover, the PSCs with $CH_3NH_3PbI_xCl_{3-x}$:ZnO bulk heterojunction exhibit high fill factor of 77.3% and short current density of 22.71 mA cm^{-2}, which is attributed to improved perovskite quality. The bulk heterojunction structure is fabricated by combining perovskite and metal oxides, which is of great importance to the development and commercialization of PSCs in the future.

* Corresponding author.
** Corresponding author.
*** Corresponding author.
E-mail address: zyliu01@163.com (Z. Liu).

https://doi.org/10.1016/j.jpowsour.2018.09.007
Received 30 May 2018; Received in revised form 3 August 2018; Accepted 3 September 2018
0378-7753/

1. Introduction

The limited supply and hazards of non-renewable energy resourses made it clear indication that for sustainable environment have to switch to the renewable energy resources such as solar energy. Solar cells can convert solar energy into electricity, which became a hotspot in the field of renewable energy [1–3]. Researcher committed on exploring the photovoltaic devices with low cost and high efficiency. Since 2009, Organic-inorganic metal halide based perovskite solar cells (PSCs) have aroused wide scientific concern [4], as its power conversion efficiency (PCE) has reached 22.7% in just a few years of time [5]. PSCs have rapidly become one of the hotspots in the research due to its characteristics of high efficiency, low cost and simple preparation [6–9]. Perovskite material has many advantages over others, such as strong absorbance, appropriate band gap and bipolar carrier transport [10–13]. Due to all above reasons, PSCs are now on the verge of commercialization. The device structure of PSCs generally can be divided into two types, namely typical mesostructure and planar heterojunction structure. The planar heterojunction structure is a “sandwich structure” between n-type material and p-type material [14,15]. The n-type material and the p-type material respectively serve as an electron transport layer (ETL) and an hole transport layer (HTL). The planar heterojunction PSCs can also be classified into two types: regular n-i-p configuration (ETL/Perovskite active layer/HTL), and inverted p-i-n configuration (HTL/Perovskite active layer/ETL) [16,17]. With the advantages of low-temperature preparation and sharply-reduced hysteresis and reduced thickness of active layer the inverted planar heterojunction PSCs has been regarded as one of the most potential assembly for commecialization [18,19]. However, much work remains to be done to promote the commercialization of PSCs, such as minimizing toxicity, improving stability and enhancing carrier extraction efficiency, etc [20,21].

Zinc oxide (ZnO) is one of the most electron-selective materials and electron transport materials used in regular planar heterojunction PSCs this is because ZnO possesses a low band position and high electron mobility [22]. Moreover, ZnO is also able to form various nanostructures under different preparation conditions, such as nanoparticles, nanowires and nanorods [23]. Until now, the PCE of PSCs with ZnO ETL has exceeded 16%, due to efficient charge extraction and carriers transport of ZnO material [24,25]. Particularly, ZnO nanoparticles play an important role as an ETL material of PSCs. Although ZnO has been used in inverted planar PSCs [26,27], an issue of the application of ZnO in inverted planar heterojunction PSCs has not been studied deeply. For this reason, this study paved a new route to prepare an inverted plane PSC with $CH_3NH_3PbI_{3-x}Cl_x$:ZnO bulk heterojunction via blending ZnO nanoparticles with $CH_3NH_3PbI_{3-x}Cl_x$ precursor solution. The purposes of the work are to prepare perovskite films with high performance by adding ZnO nanoparticles and to enhance electron transporting properties of cells by forming $CH_3NH_3PbI_{3-x}Cl_x$:ZnO bulk heterojunction. The perovskite film with large grain is obtained by adding ZnO nanoparticles appropriately. At the same time, the photoelectric properties of the device has significantly improved. The conductivity and electron mobility of the $CH_3NH_3PbI_{3-x}Cl_x$:ZnO film is better than that of $CH_3NH_3PbI_{3-x}Cl_x$ film. As a result, a maximum PCE of 17.26% with an open circuit voltage (V_{OC}) of 0.98 V, a short circuit current density (J_{SC}) of 22.71 mA cm^{-2}, and a fill factor (FF) of 77.3% has been achieved.

2. Experiments

2.1. Materials and preparation

ZnO nanoparticles were purchased from Shanghai Chemical Industry Co. Poly (3, 4-ethylene dioxy-thiophene)–poly (styrene sulfonate) (PEDOT:PSS) was bought from Heraeus (Germany). Phenyl-C_{61}-butyric acid methyl ester (PCBM) and 4, 7-Diphenyl-1, 10-phenanthroline (Bphen) were produced in Nichem Fine Technology Co., Ltd. (Taiwan). CH_3NH_3I was synthesized by CH_3NH_2 and HI, according to the previously reported procedure [28]. PCBM solutions and Bphen solutions were prepared according to methods mentioned above [29]. The ZnO solution was manufactured by dissolving ZnO nanoparticles into DMF in varying proportions and stirring the mixture for 12 h. As shown in Fig. S1, with the increase in amount of ZnO, the color of mixed DMF solvent gradually turns white. $CH_3NH_3PbI_{3-x}Cl_x$ precursor solution was fabricated by solubilizing CH_3NH_3I and $PbCl_2$ in DMF solvent with a molar ratio of 3:1 [30,31] and stirring the compound at 60 °C for 12 h.

2.2. Fabrication of the device

Indium tin oxide (ITO) coated glass (Fine Chemicals Industry Co., 10 Ω sq^{-1}) was etched and cleaned according to methods mentioned above [32], PEDOT:PSS film was spin-coated onto the ITO substrate at 4500 rpm for 40 s and then annealed at 140 °C for 20 min. The $CH_3NH_3PbI_{3-x}Cl_x$ precursor solution was spin-coated onto the PEDOT:PSS film at 4000 rpm for 40 s in a N_2 glove box. The annealing of wet perovskite films was carried out by adopting a typical gradient increased temperature method [33–35]. Then, PCBM solution and Bphen solution were deposited by spin-coating at 2000 rpm for 40 s. Finally, Ag film was thermally deposited under vacuum at 4.5×10^{-4} Pa through a shadow mask.

2.3. Characterizations

The surface morphology of perovskite films and section morphology of PSC were characterized by a field emission scanning electron microscope (FESEM) (Quanta 200 FEG, FEI Co.). Energy dispersive spectroscopy was conducted through the EDS device connected to FESEM. The TEM images of ZnO nanoparticles and perovskite crystals are measured by an FEI Talos (S) transmission electron microscopy (TEM) at 200 kV. The steady-state and time-resolved steady-state photoluminescence (PL) were measured by using an Edinburgh FLS980 fluorescence spectrophotometer with an excitation at 400 nm. The crystalline phase and X-ray diffraction (XRD) patterns of perovskite films were recorded on a Rigaku D/MAX-2400 diffractometer. UV–Vis absorption and reflection spectra measurements of perovskite films were carried out by using Shimadzu UV-2550 spectrometer. The capacitance-voltage (C−V) characteristics were performed by Agilent 4284 A LCR Meter. X-ray photoelectron spectroscopy (XPS) was measured via AXIS Ultra instrument (Kratos UK). The current density-voltage (*J-V*) curves were measured (2400 Series Source Meter, Keithley Instruments) under simulated Air-Mass (AM) 1.5 sunlight at 100 mW cm^{-2} (Newport, Class AAA solar simulator, 94023A-U). The incident-photon-to-current efficiency (IPCE) measurement was performed by adopting a system composed of xenon lamp, monochromator, chopper, lock-in amplifier and calibrated silicon photodetector.

3. Results and discussion

Fig. 1a represents the schematic crossection of fabricated p-i-n planar perovskite solar cell with device configuration of ITO/PEDOT:PSS/$CH_3NH_3PbI_{3-x}Cl_x$: ZnO (300 nm)/Bphen/Ag. The associated cross-section FESEM image of the device with $CH_3NH_3PbI_{3-x}Cl_x$:ZnO bulk heterojunction has been represented in Fig. 1b. PEDOT:PSS is selected as an HTL due to its efficient charge extraction [36]. Bphen is served as the modification layer becasue it can make the Ag cathode interface flat and smooth [37].

3.1. Photovoltaic performance of devices

The ZnO nanoparticles are mixed with $CH_3NH_3PbI_{3-x}Cl_x$ precursor solutions in varying proportions in order to find the optimal proportion

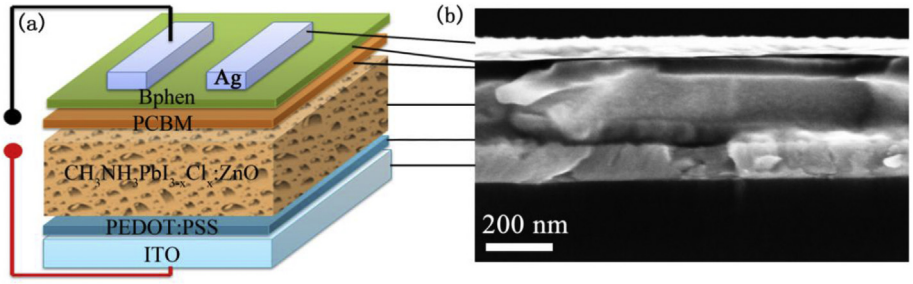

Fig. 1. (a) The schematic illustration and (b) the cross-section FESEM image of the PSC device with $CH_3NH_3PbI_xCl_{3-x}$:ZnO film.

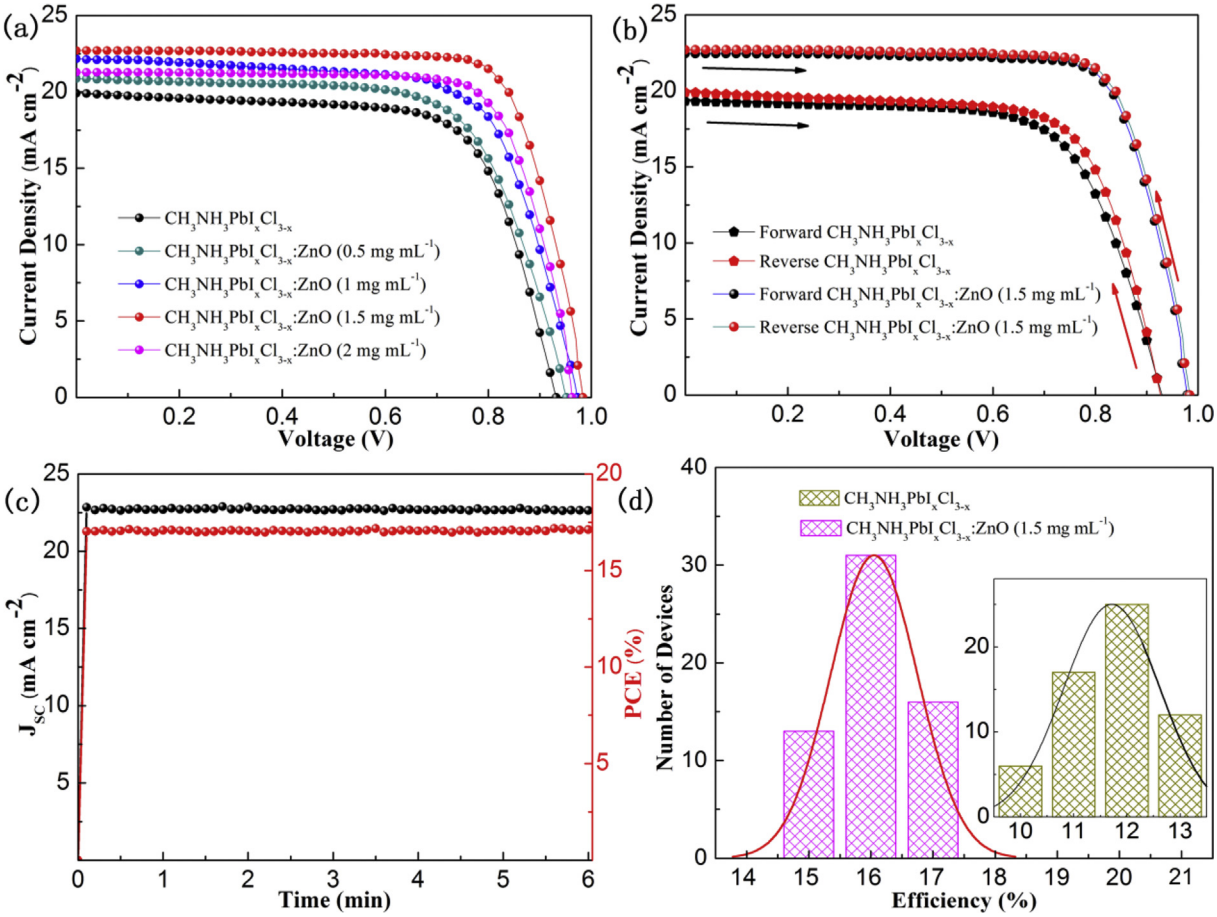

Fig. 2. (a) The *J–V* curves of cells with $CH_3NH_3PbI_xCl_{3-x}$:ZnO (0, 0.5, 1, 1.5 and 2 mg mL^{-1}) films. (b) The *J–V* curves (reverse and forward) of cells with $CH_3NH_3PbI_xCl_{3-x}$:ZnO (1.5 mg mL^{-1}) and $CH_3NH_3PbI_xCl_{3-x}$ films. (c) The steady-state photocurrent and efficiency are measured at the maximum power point (0.80 V) of cell with $CH_3NH_3PbI_xCl_{3-x}$:ZnO film. (d) The histogram of PCEs of 60 cells with $CH_3NH_3PbI_xCl_{3-x}$:ZnO (1.5 mg mL^{-1}) films. Inset: the histogram of PCEs of 60 cells with $CH_3NH_3PbI_xCl_{3-x}$ films.

for improved performance of solar cells. Fig. 2a shows the performance of $CH_3NH_3PbI_xCl_{3-x}$:ZnO active layer-based PSCs obtained with different concentrations of ZnO nanoparticles (0, 0.5, 1, 1.5 and 2 mg mL^{-1}) in $CH_3NH_3PbI_{3-x}Cl_x$ precursor solutions under AM 1.5 G conditions (100 mW cm^{-2}). The photovoltaic performance parameters of devices are represented in Table S1. The reference device based on $CH_3NH_3PbI_{3-x}Cl_x$ precursor solutions without ZnO nanoparticles exhibited a PCE of 12.63% with V_{OC} of 0.93 V, J_{SC} of 19.87 mA cm^{-2} and FF of 68.7%. The performance of cell is heavily dependent on the amount of ZnO nanoparticles added. Under the condition of ZnO concentration of 1.5 mg mL^{-1}, the best cell performance with PCE of 17.26%, V_{OC} of 0.98 V, J_{SC} of 22.71 mA cm^{-2} and FF of 77.3% has been achieved. In order to analyze the hysteresis behavior of devices, the devices are measured by applying a forward and reverse bias at a scan rate of 0.01 V/s. The hysteresis curves of devices with $CH_3NH_3PbI_xCl_{3-x}$ and $CH_3NH_3PbI_xCl_{3-x}$:ZnO (1.5 mg mL^{-1}) film have been shown in Fig. 2b. Compared with the device with $CH_3NH_3PbI_xCl_{3-x}$ film, the device with $CH_3NH_3PbI_xCl_{3-x}$:ZnO (1.5 mg mL^{-1}) film show a weaker hysteresis. To further confirm the reliability of PSCs with ZnO nanoparticles, the steady-state photocurrent and efficiency is measured at the maximum power point (0.80 V) and shown in Fig. 2c. The steady-state J_{SC} of 22.67 mA cm^{-2} and PCE of 17.22% are very close to the value obtained from the *J–V* curve measurements, suggesting that the photocurrent hysteresis of the cells can be suppressed by inserting ZnO nanoparticles. Fig. 2d shows the histograms and Gaussian distributions of PCE parameters based on 60 cells with $CH_3NH_3PbI_xCl_{3-x}$:ZnO (1.5 mg mL^{-1}) and without ZnO have been researched respectively. The relative standard deviation of cells with $CH_3NH_3PbI_xCl_{3-x}$:ZnO

(1.5 mg mL^{-1}) is lower than that of ones with $CH_3NH_3PbI_xCl_{3-x}$ (inset), indicating that the reproducibility of the former is better. The long-term stability of the PSCs with $CH_3NH_3PbI_xCl_{3-x}$ and $CH_3NH_3PbI_xCl_{3-x}$:ZnO (1.5 mg mL^{-1}) is tested and shown in Fig. S2. The devices with $CH_3NH_3PbI_xCl_{3-x}$:ZnO (1.5 mg mL^{-1}) film still maintains a 16.86% of PCE after 960 h degradation, which is more than 97% of the initial PCE value. However, the PCE of the devices with $CH_3NH_3PbI_xCl_{3-x}$ film just maintains 86% of the initial one. It can be speculated that the excellent stability of PSC with $CH_3NH_3PbI_xCl_{3-x}$:ZnO (1.5 mg mL^{-1}) film is attributed to dense perovskite film.

A remarkable improvement in the performance of PSCs with ZnO nanoparticles is partly because of a marked increase in the current density. As shown in Fig. S3, The IPCE spectra measurement of PSCs with $CH_3NH_3PbI_xCl_{3-x}$ film and $CH_3NH_3PbI_xCl_{3-x}$:ZnO (1.5 mg mL^{-1}) film has been conducted to clearly reveal the increase in current density. The cell with $CH_3NH_3PbI_xCl_{3-x}$:ZnO (1.5 mg mL^{-1}) shows higher IPCE intensity, and a progressive enhancement in nearly entire visible light range can be observed. The J_{SC} of 22.57 mA cm^{-2} is calculated via IPCE intensity of the cell with $CH_3NH_3PbI_xCl_{3-x}$:ZnO (1.5 mg mL^{-1}), which is very consistent with the J_{SC} of 22.71 mA cm^{-2} obtained from the *J–V* curve. Light harvesting efficiency of cells has a positive correlation with the absorption value of perovskite films. As shown in Fig. 3a, the $CH_3NH_3PbI_xCl_{3-x}$ and $CH_3NH_3PbI_xCl_{3-x}$:ZnO (1.5 mg mL^{-1}) films show slightly different light absorption, according to the UV–vis measurement results. Apparently, perovskite film with 1.5 mg mL^{-1} ZnO demonstrates a higher absorption in the visible light range of 300–800 nm. Moreover, when the perovskite film is covered with a layer of Ag film, the light absorption of $CH_3NH_3PbI_xCl_{3-x}$ and $CH_3NH_3PbI_xCl_{3-x}$:ZnO (1.5 mg mL^{-1}) films shows a large difference. Fig. 3b shows the absorption spectrum and reflectance spectrum of ZnO nanoparticles. It is known that ZnO has a high light absorption in the wavelength range less than 400 nm [38]. Therefore, the improved light absorption of the perovskite film with ZnO nanoparticles over the entire wavelength band is not only the contribution of light absorption by ZnO but also improved perovskite film. At the same time, Fig. 3b shows clearly that ZnO has a high reflectance in the wavelength range of 400–800 nm. As demonstrated in Fig. 3c, the promoting effect of ZnO nanoparticles on the absorption of perovskite film can come from two aspects. 1) ZnO nanoparticle acts as reflection centers. When sunlight reaches the perovskite layer, the light reflected by the ZnO can be absorbed by the surrounding perovskite. 2) The back contact reflector is made of ZnO nanoparticles and Ag film, leading to an increased absorption in the perovskite film [39]. It is observed that the moderate ZnO nanoparticles in the perovskite film play an important role in improving light harvesting efficiency of cell [40]. On the contrary, an excess of ZnO nanoparticles would be detrimental to the crystallization of perovskites, resulting in a poor light absorption and low current densities. What's more, the band gap (Fig. S4) of the film is obtained by according to the absorption spectrum in Fig. 3a. When a small amount of ZnO nanoparticles are added to the perovskite film, no significant change is found in the absorption spectrum. It is possible that a small amount of ZnO nanoparticles does not change the crystal structure of the perovskite, which is consistent with the results of the XRD pattern mentioned below.

3.2. The performance of $CH_3NH_3PbI_{3-x}Cl_x$:ZnO film

The performance of PSCs has been enhanced by optimizing perovskite film. The surface morphology FESEM images of perovskite films with different ZnO concentrations are represented in Fig. 4a–h. The statistical results of perovskite grain size are shown in Fig. S5. It is seen that the size of the perovskite crystal grains gradually increases with the ZnO concentration. The average grain sizes of the perovskite crystals with different ZnO concentrations respectively are 1.38 μm

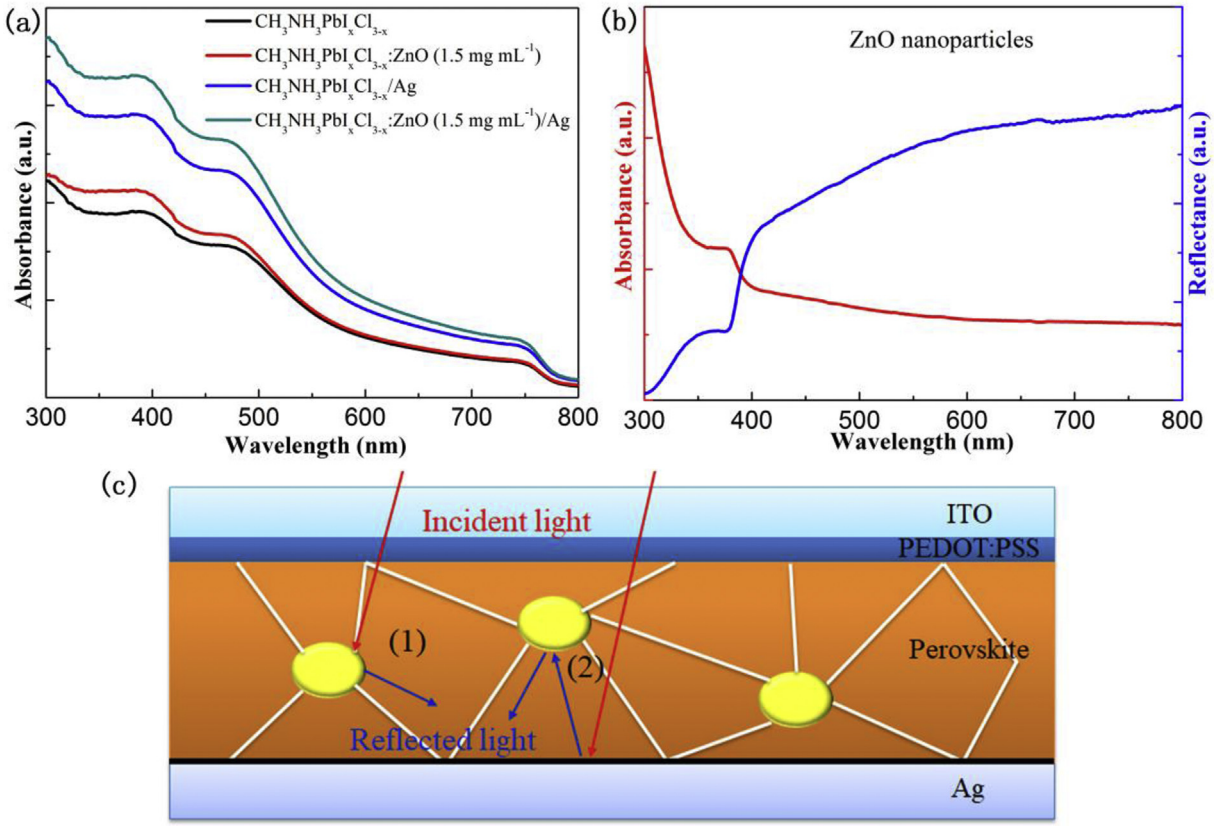

Fig. 3. The absorption spectra of $CH_3NH_3PbI_xCl_{3-x}$ film and $CH_3NH_3PbI_xCl_{3-x}$:ZnO film (1.5 mg mL^{-1}) (b) The absorption spectrum and reflectance spectrum of ZnO nanoparticles. (c) The Schematic illustration of function that the light absorption of the perovskite film is promoted by the ZnO nanoparticles.

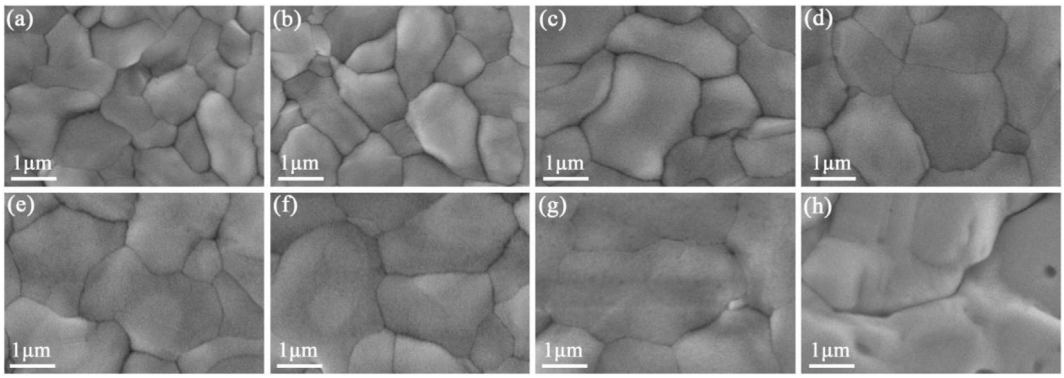

Fig. 4. The FESEM images of perovskite films with different concentration of ZnO nanoparticles (a) 0 mg mL^{-1}, (b) 0.1 mg mL^{-1}, (c) 0.2 mg mL^{-1}, (d) 0.5 mg mL^{-1}, (e) 1 mg mL^{-1} (f) 1.5 mg mL^{-1} (g) 2 mg mL^{-1} and (h) 5 mg mL^{-1}.

(0 mg mL^{-1}), 1.49 μm (0.1 mg mL^{-1}), 1.89 μm (0.2 mg mL^{-1}), 2.27 μm (0.5 mL^{-1}), 2.43 μm (1 mg mL^{-1}), 2.58 μm (1.5 mg mL^{-1}), 2.82 μm (2 mg mL^{-1}), 2.88 μm (5 mg mL^{-1}), respectively. The larger perovskite grains are capable of avoiding the energy loss in the photovoltaic process, leading to a high V_{OC} [41–43]. The changes in the perovskite film morphology can be attributed to the polarity of ZnO. The dipole moments of ZnO and CH_3NH_3 are 6.01 D and 2.29 D respectively, which could be evaluated via the Gaussian [44]. Because ZnO has a larger dipole moment than CH_3NH_3, moderate ZnO nanoparticles can effectively facilitate the assemblage of monomer and polymer [45,46]. What's more, previous report has also shown that appropriate amount of ZnO nanoparticles can improve the morphology of the perovskite film [47]. However, an excess of ZnO nanoparticle makes perovskite film produce large voids, resulting in a poor device performance. In addition, the grain growth mechanism of perovskite film with ZnO nanoparticles might be similar to the perovskite with V_2O_x or TiO_2 [29,48]. ZnO nanoparticles with the size of 30–50 nm have been reported to help obtain high-quality perovskite films [49]. ZnO nanoparticles dispersed in perovskite precursor solution provide some nucleation sites, accelerating grain growth of the perovskite [50]. The continuous growth of small grains and migration of the crystal boundaries lead to a gradual increase in grain size [51].

The XRD patterns of $CH_3NH_3PbI_xCl_{3-x}$:ZnO (0.5, 1, 1.5 and 2 mg mL^{-1}) films on the ITO/PEDOT:PSS substrates have been measured to further analyze the role of ZnO nanoparticles in perovskite film. As shown in Fig. S6a, two strong diffraction peaks corresponding to (110) and (220) planes have been observed at $2\theta = 14.14^{\circ}$ and 28.48° respectively [28,52]. Table S2 gives a detailed description of the diffraction intensity and the full width of half maximum (FWHM) of two diffraction peaks. It is clearly evident that the intensity of diffraction peaks becomes stronger with the augment in ZnO concentration, implying that the overall crystallinity of the perovskite phase has been increased significantly. At the same time, the FWHM of diffraction peaks decline gradually with the increase in ZnO concentration. The smaller FWHM of diffraction peaks, the larger grains of peovskite will be, which is very consistent with the results shown in FESEM (Fig. 4). The positions of diffraction peaks can hardly be changed in the XRD pattern, suggesting that the crystal structure of perovskite is steady and well-preserved. It is worth noting that the diffraction peaks of ZnO do not exist in the XRD patterns of perovskites films, comparing the XRD patterns of ZnO nanoparticles (Fig. S6b). The amount of ZnO nanoparticles are too few to be detected, compared to the crystallite sites of $CH_3NH_3PbI_{3-x}Cl_x$.

The XPS is employed to further understand the relation of ZnO nanoparticles to the improved crystallization of perovskite films. The XPS spectra of $CH_3NH_3PbI_xCl_{3-x}$:ZnO films (0.5, 1, 1.5 and 2 mg mL^{-1}) are measured. As shown in Fig. S7, two peaks at the binding energy of 1044.1 eV and 1021.1 eV are corresponding to the $2p_{1/2}$ and $2p_{3/2}$ doublets of Zn respectively. The position of the $2p_{1/2}$ and $2p_{3/2}$ doublets of Zn in the perovskite film is the same as that of in ZnO nanoparticles. Furthermore, there is no significant changes in binding energy positions of Zn in the perovskite films with different ZnO concentrations. The peak intensity boosts with the ZnO concentration, demonstrating that ZnO does exist in the perovskite film. In addition, the energy dispersive spectroscopy (EDS) analysis has been performed on the $CH_3NH_3PbI_xCl_{3-x}$:ZnO (1.5 mg mL^{-1}) film on the Glass/ITO/PEDOT:PSS. The surface and cross-section FESEM images with elemental mappings, and EDS spectrum are shown in Fig. 5a–e. As expected, an additional signal of Zn element has been observed in the EDS spectra. The signals of the other elements presumably derive from the glass, ITO and ZnO, including Ca, Na, Mg, Si and O element. The distribution of Zn element is uniform both in the surface mappings and the cross-section ones, which manifests that the ZnO nanoparticles are evenly distributed in the perovskite film.

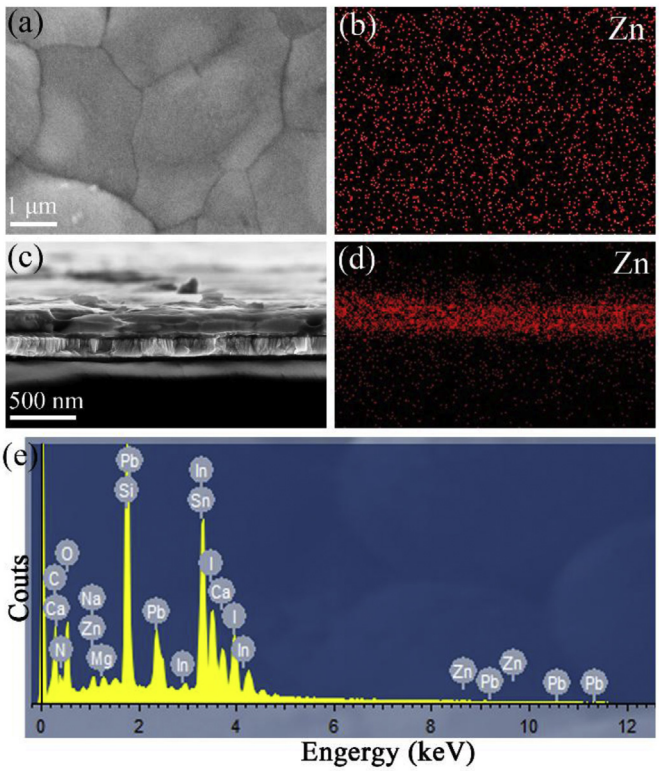

Fig. 5. The (a) surface and (c) cross-section FESEM images with (b and d) elemental mappings, and (e) EDS spectrum of $CH_3NH_3PbI_xCl_{3-x}$:ZnO (1.5 mg mL^{-1}) films.

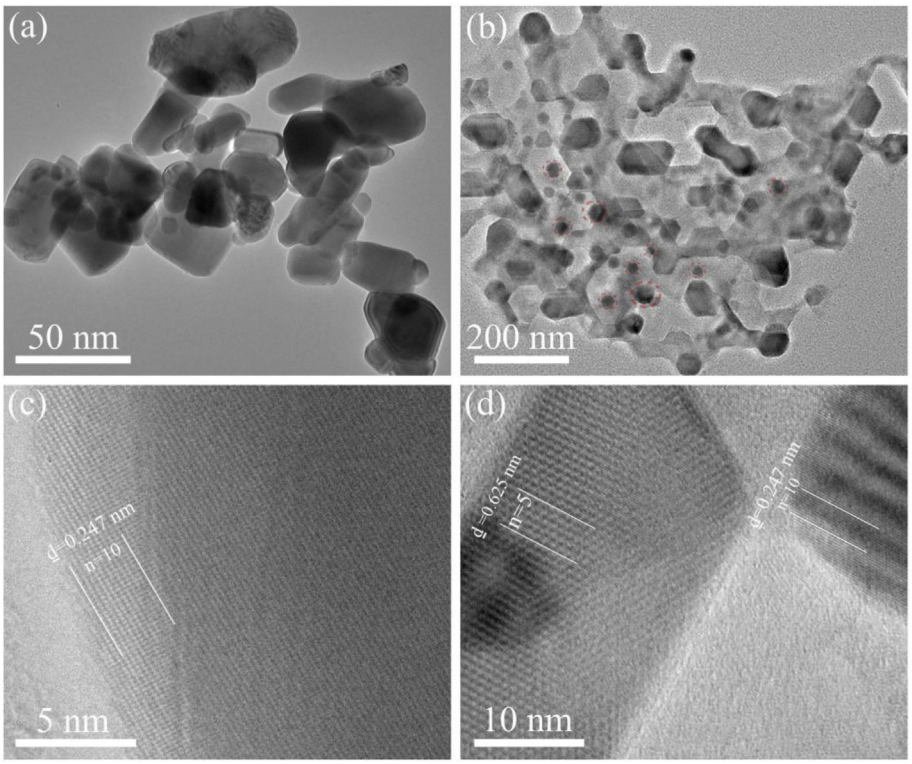

Fig. 6. The TEM images of ZnO nanoparticles (a and c), the images of $CH_3NH_3PbI_xCl_{3-x}$:ZnO (b and d). The lattice spacings of (101) crystal plane of ZnO and (110) crystal plane of perovskite are measured and marked.

3.3. The role of $CH_3NH_3PbI_{3-x}Cl_x$:ZnO bulk heterojunction

There is no doubt that ZnO can improve the optoelectronic performance of PSC devices. However, Some previous reports claim that ZnO can react with perovskite and result in the degradation of perovskite film [53,54], because hydroxide on the surface of ZnO could destroy the crystal structure of perovskite. In this study, the problem can be solved very well. Before the ZnO nanoparticles are mixed into the perovskite film, they are dispersed in the N, N-dimethylformamide (DMF) solution. As shown in Fig. S8a-b, before being dispersed in the DMF solvent, ZnO nanoparticles can be seen in the XPS spectrum that the O1s orbital peak is formed by the superposition of the peaks of O^{2-} and OH^-. However, after the ZnO nanoparticles are dispersed in the DMF solvent, no peak of OH^- is seen in the XPS spectrum. Hydroxy radicals that may be present on the surface of ZnO are reacted by DMF [55], so the perovskite crystals can hardly be destroyed. The solubility of ZnO in DMF is limited, thus ZnO nanoparticles are adsorbed on the surface of $CH_3NH_3PbI_xCl_{3-x}$ crystals, or are encased in the bulk of $CH_3NH_3PbI_xCl_{3-x}$ crystals. The TEM micrographs of ZnO nanoparticles and $CH_3NH_3PbI_xCl_{3-x}$:ZnO are shown in Fig. 6a–d. The ZnO nanoparticles with the size of about 40 nm (red dotted line) have been found in $CH_3NH_3PbI_xCl_{3-x}$ crystals (Fig. 6b), which is in accordance with the EDS elemental analysis. The lattice spacings of ZnO and $CH_3NH_3PbI_xCl_{3-x}$ are 0.247 nm and 0.625 nm, respectively, which correspond to the (101) crystal plane of ZnO and the (110) crystal plane of $CH_3NH_3PbI_xCl_{3-x}$ (Fig. 6d).

The PL of $CH_3NH_3PbI_{3-x}Cl_x$, $CH_3NH_3PbI_xCl_{3-x}$/PCBM, $CH_3NH_3PbI_xCl_{3-x}$:ZnO (1.5 mg mL^{-1}) and $CH_3NH_3PbI_xCl_{3-x}$:ZnO (1.5 mg mL^{-1})/PCBM films on glass substrates are gauged through 400 nm laser. As shown in Fig. 7a, all of four films exhibit the same photoluminescence peak position of 763 nm, which indicates that the PL is determined by the band gap of perovskite. The PL intensity of the $CH_3NH_3PbI_{3-x}Cl_x$:ZnO film is much weaker than that of $CH_3NH_3PbI_xCl_{3-x}$ film without ZnO nanoparticles, implying that the bulk heterojunction does exist in the $CH_3NH_3PbI_{3-x}Cl_x$:ZnO film. The $CH_3NH_3PbI_{3-x}Cl_x$:ZnO bulk heterojunction in the perovskite film makes the generated exciton reach heterojunction interface through a very short transmission path, thereby dramatically improving the efficiency of charge separation. The steady state PL intensity of the $CH_3NH_3PbI_{3-x}Cl_x$:ZnO film is not completely quenched, manifesting that ZnO nanoparticles in $CH_3NH_3PbI_{3-x}Cl_x$:ZnO film is not sufficient for charge separation of the excitons or electron transport. Therefore the PCBM electron transport layer film is spin-coated on the surface of the $CH_3NH_3PbI_{3-x}Cl_x$:ZnO film. The PL quenching efficiency [56] of $CH_3NH_3PbI_xCl_{3-x}$, $CH_3NH_3PbI_xCl_{3-x}$/PCBM, $CH_3NH_3PbI_xCl_{3-x}$:ZnO (1.5 mg mL^{-1}) and $CH_3NH_3PbI_xCl_{3-x}$:ZnO (1.5 mg mL^{-1})/PCBM films are listed in Table 1. $CH_3NH_3PbI_xCl_{3-x}$:ZnO/PCBM film shows the highest quenching, which is well reflected in the photovoltaic performance of devices made implying this layer. To exclude the possibility that the complete PL quench results from the charge carrier recombination brought about by the defect at the $CH_3NH_3PbI_xCl_{3-x}$:ZnO/PCBM, the charge injection/separation behavior of the $CH_3NH_3PbI_xCl_{3-x}$/PCBM and $CH_3NH_3PbI_xCl_{3-x}$:ZnO/PCBM is compared. The time-resolved PL decay of $CH_3NH_3PbI_xCl_{3-x}$/PCBM and $CH_3NH_3PbI_xCl_{3-x}$:ZnO/PCBM films on glass substrates are measured and shown in Fig. 7b. The decay curves of two films are fitted by a double exponential function. The $CH_3NH_3PbI_xCl_{3-x}$:ZnO (1.5 mg mL^{-1})/PCBM film exhibits a reduced PL lifetime of 63 ns, compared with the $CH_3NH_3PbI_xCl_{3-x}$/PCBM film (127 ns). The PL quenching of $CH_3NH_3PbI_xCl_{3-x}$:ZnO/PCBM film is faster than that of $CH_3NH_3PbI_xCl_{3-x}$/PCBM film, indicating a faster transfer of charge carrier from $CH_3NH_3PbI_xCl_{3-x}$:ZnO film to PCBM film. This further indicates that the charge injection from $CH_3NH_3PbI_xCl_{3-x}$:ZnO to PCBM film is more efficient than that from $CH_3NH_3PbI_xCl_{3-x}$ to PCBM film, resulting in a major enhancement in the charge extraction of PSCs.

Carrier dynamics of PSCs is further studied by using transient photocurrent and transient photovoltage technique [57,58]. The transient photovoltage decay measurements of two devices can be observed in Fig. 7c. The photocurrent delay time of the device with $CH_3NH_3PbI_xCl_{3-x}$:ZnO is shorter than that of the one with $CH_3NH_3PbI_xCl_{3-x}$, suggesting that the electron carrier extraction ability

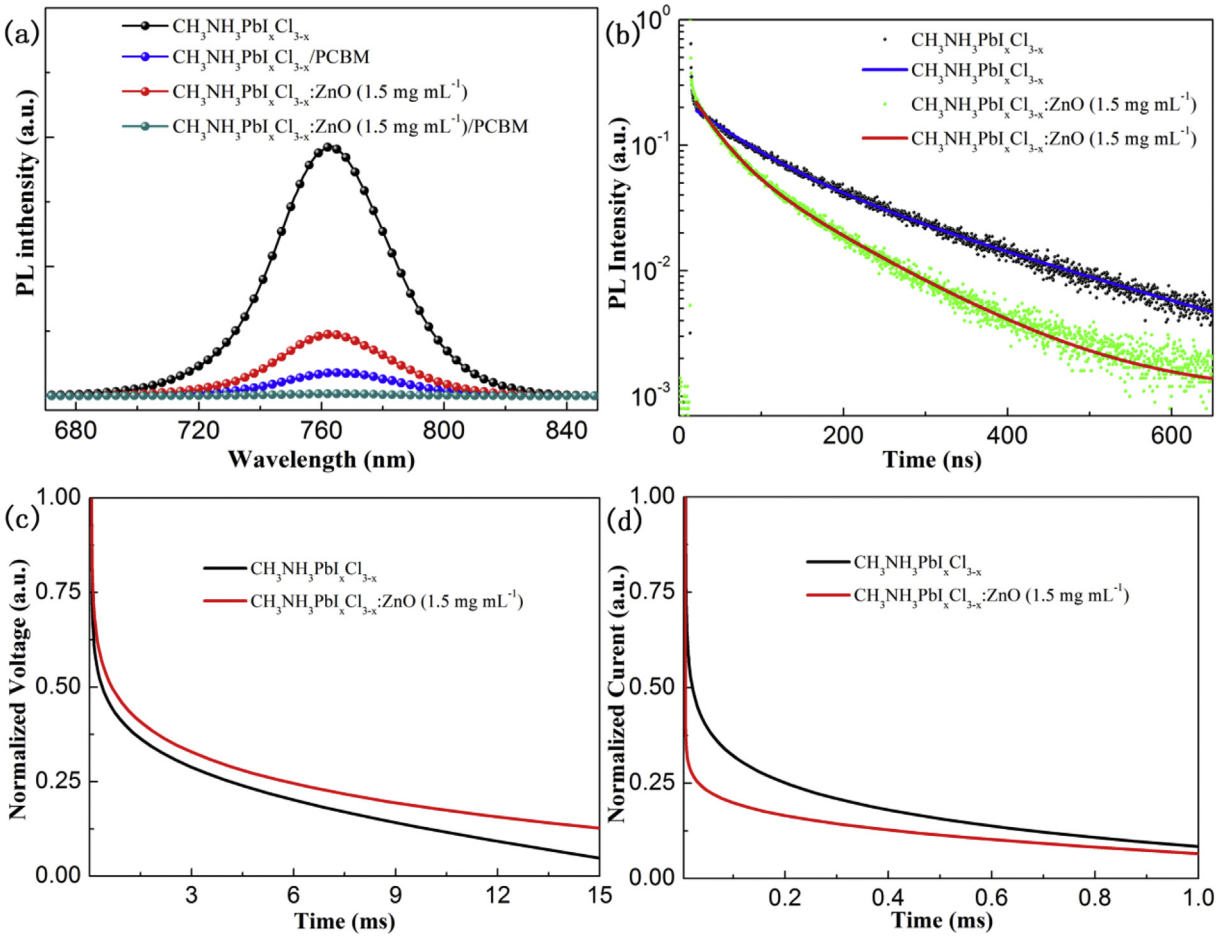

Fig. 7. The steady-state PL spectra of $CH_3NH_3PbI_{3-x}Cl_x$, $CH_3NH_3PbI_xCl_{3-x}$/PCBM, $CH_3NH_3PbI_xCl_{3-x}$: ZnO (1.5 mg mL^{-1}) and $CH_3NH_3PbI_xCl_{3-x}$:ZnO (1.5 mg mL^{-1})/PCBM films on glass substrates. (b) The time-resolved PL spectra of $CH_3NH_3PbI_xCl_{3-x}$/PCBM and $CH_3NH_3PbI_xCl_{3-x}$:ZnO/PCBM films on glass substrates. The (c) transient photovoltage decay and (d) photocurrent of cells with $CH_3NH_3PbI_xCl_{3-x}$:ZnO (1.5 mg mL^{-1}) and $CH_3NH_3PbI_xCl_{3-x}$ films.

of the former is better, thus the results matches well with the steady-state PL and time-resolved PL results. In addition, Fig. 7d shows transient photovoltage decay measurements of two devices made using $CH_3NH_3PbI_xCl_{3-x}$ and $CH_3NH_3PbI_xCl_{3-x}$:ZnO active layers. The lifetimes are represented in single exponential fitting of decay curves of perovskite reference and integrated devices. The photovoltage decay curves of two devices are fitted by a single exponential function. The photovoltage decay of the device with $CH_3NH_3PbI_xCl_{3-x}$:ZnO is slower than that of the one with $CH_3NH_3PbI_xCl_{3-x}$, resulting in a significant improved carrier lifetime and a decrease of charge carrier recombination velocity, which demonstrates that the carrier diffusion length has been improved. The long carrier diffusion length results from high charge collection efficiency, leading to high J_{SC} of PSCs with $CH_3NH_3PbI_xCl_{3-x}$:ZnO.

The photocurrent density of PSCs is largely determined by light-harvesting efficiency, charge collection efficiency and charge injection/transfer efficiency, which might be closely associated with carrier diffusion length, conductivity of perovskite layer and carrier mobility. According to the method mentioned above [59], the conductivity of various perovskite films is measured by putting the film between ITO and Ag electrodes. According to the equation: $\sigma = \frac{1}{R}\cdot\frac{L}{S}$, where σ, L, S and R respectively represent conductivity, the thickness (300 nm) of perovskite film, area (0.0625 cm^{-2}) of single Ag electrode and resistance of perovskite film. The conductivity of $CH_3NH_3PbI_xCl_{3-x}$ and $CH_3NH_3PbI_xCl_{3-x}$:ZnO (1.5 mg mL^{-1}) films can be calculated from the I−V curves shown in Fig. 8a. The conductivity of $CH_3NH_3PbI_xCl_{3-x}$:ZnO film (0.014 mS cm^{-1}) is higher than that of $CH_3NH_3PbI_xCl_{3-x}$ film (0.008 mS cm^{-1}). The electrical conductivity of the perovskite film is proportional to both the carrier mobility and carrier density. And it can be represented by the equation $\sigma = Ne\mu$, where σ, N, e, and μ respectively represent electrical conductivity, carrier density, elementary charge and carrier mobility [60]. To investigate the impact of perovskite film with ZnO nanoparticles on the charge carrier density of PSCs, C−V characteristics of the devices are measured (Fig. S9). The carrier density N of the PSCs can be estimated by calculating the slope of $1/C^2$ versus applied voltage graph by the equation: $N = \left(\frac{2}{q\varepsilon\varepsilon_0 A^2}\right) dV/d(1/C^2)$ [61,62], where ε, ε_0, A and C respectively represent the dielectric constant of the material, the permittivity of free space, the area of the device, and the capacitance. It can be found that the PSC with $CH_3NH_3PbI_xCl_{3-x}$:ZnO (1.5 mg mL^{-1}) film has higher

Table 1
PL quenching efficiency of $CH_3NH_3PbI_xCl_{3-x}$, $CH_3NH_3PbI_xCl_{3-x}$/PCBM, $CH_3NH_3PbI_xCl_{3-x}$: ZnO (1.5 mg mL^{-1}) and $CH_3NH_3PbI_xCl_{3-x}$: ZnO (1.5 mg mL^{-1})/PCBM films.

Sample	$CH_3NH_3PbI_xCl_{3-x}$	$CH_3NH_3PbI_xCl_{3-x}$/PCBM	$CH_3NH_3PbI_xCl_{3-x}$: ZnO (1.5 mg mL^{-1})	$CH_3NH_3PbI_xCl_{3-x}$: ZnO (1.5 mg mL^{-1})/PCBM
PL intensity	17371	1631	4305	152
PL intensity quenching (%)	0	90.6	75.2	99.1

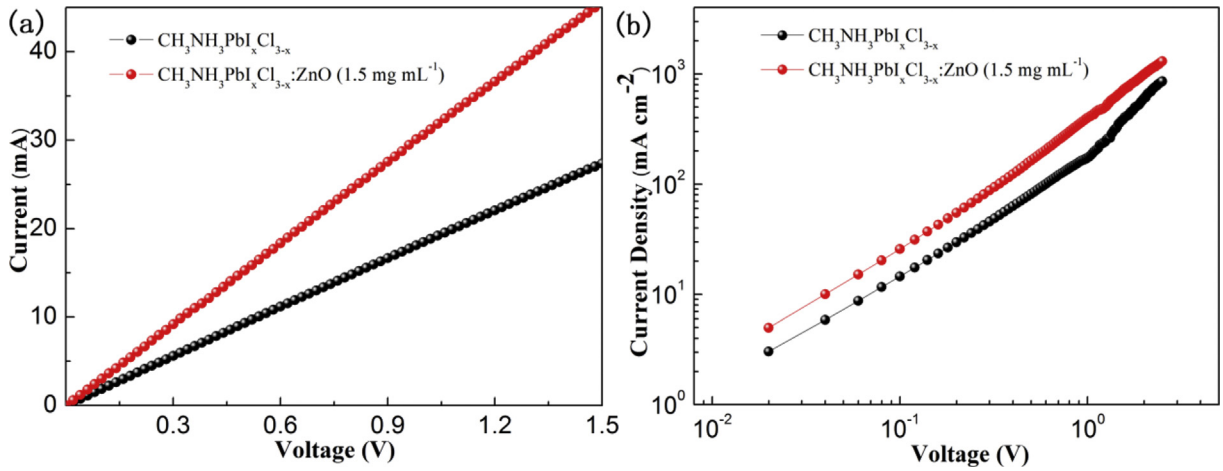

Fig. 8. (a) The I–V curves of the devices with the configuration of ITO/$CH_3NH_3PbI_{3-x}Cl_x$:ZnO (1.5 mg mL^{-1}) or $CH_3NH_3PbI_{3-x}Cl_x$/Ag. (b) The typical double logarithmic *J-V* characteristics of two devices with the configuration of ITO/$CH_3NH_3PbI_{3-x}Cl_x$:ZnO (1.5 mg mL^{-1}) or $CH_3NH_3PbI_{3-x}Cl_x$/PCBM/Ag.

carrier density compare with the PSC with $CH_3NH_3PbI_xCl_{3-x}$ film. The perovskite film with high carrier concentration facilitates the transport of charge in the PSC device. The devices with the structure of ITO/Perovskite (300 nm)/PCBM/Ag are fabricated to probe into the electrical properties of perovskite films. The electron mobility of $CH_3NH_3PbI_xCl_{3-x}$ and $CH_3NH_3PbI_xCl_{3-x}$:ZnO (1.5 mg mL^{-1}) films has been measured via a space-charge limited current (SCLC) model [63]. Fig. 8b gives a full description of the typical double logarithmic *J-V* characteristics of two devices. The *J-V* curves make it even clear that the presence of ZnO nanoparticles in perovskite films can lead to a remarkable improvement in electron mobility which ultimately leads to the efficient electron transport properties.

4. Conclusion

In summary, the novel-technique and high-performance inverted plane PSCs with $CH_3NH_3PbI_{3-x}Cl_x$:ZnO bulk heterojunction have been prepared by adding ZnO nanoparticles to $CH_3NH_3PbI_{3-x}Cl_x$ precursor solution. The fine tuning of concentration of ZnO nanoparticles within $CH_3NH_3PbI_{3-x}Cl_x$ lead to the improved perovskite film quality as seen from XRD, UV–visible and XPS measurements. The improved perovskite film quality shown improved electron mobility and charge extraction as seen from steady state and time resolved PL measurements. As the results of this PSCs with PCE of 17.26% (hysteresis-free) with a remarkably high fill factor and short current density, when 1.5 mg mL^{-1} ZnO nanoparticles are added to $CH_3NH_3PbI_{3-x}Cl_x$ precursor solution. An excellent photoelectric property of the PSCs based on the $CH_3NH_3PbI_{3-x}Cl_x$:ZnO bulk heterojunction is mainly attributed to the high conductivity and electron mobility of $CH_3NH_3PbI_{3-x}Cl_x$:ZnO film. A brand new method of improving optoelectronic properties of PSCs via bulk heterojunction structure composed of perovskite and inorganic matter has been provided in this paper.

Acknowledgements

Z. Liu, T. He, K. Liu, J. Yang, N. Zhang and H. Liu gratefully acknowledge financial support from the Natural Science Foundation of China (NSFC Grant No. 51502081, No.11504093 and No. 21402042). S. M. Jain acknowledge Marie Curie COFUND fellowship, Welsh Assembly Government funded Ser-Cymru Solar Project, European Union's Horizon 2020 research and innovation programme under the Marie Skłodowska-Curie grant agreement No 663830. Z. Liu and T. He contributed equally to this work.

Appendix A. Supplementary data

Supplementary data related to this article can be found at https://doi.org/10.1016/j.jpowsour.2018.09.007.

References

[1] N.S. Lewis, D.G. Nocera, Proc. Natl. Acad. Sci. Unit. States Am. 103 (2006) 15729–15735.
[2] G.W. Crabtree, N.S. Lewis, Phys. Today 60 (2007) 37–42.
[3] N.S. Lewis, Science 315 (2007) 798–801.
[4] A. Kojima, K. Teshima, Y. Shirai, T. Miyasaka, J. Am. Chem. Soc. 131 (2009) 6050–6051.
[5] F. Fu, S. Pisoni, T.P. Weiss, T. Feurer, A. Wäckerlin, P. Fuchs, S. Nishiwaki, L. Zortea, A.N. Tiwari, S. Buecheler, Adv. Sci. 170 (2017) 1700675.
[6] S.D. Stranks, G.E. Eperon, G. Grancini, C. Menelaou1, M.J.P. Alcocer, T. Leijtens, L.M. Herz, A. Petrozza, H.J. Snaith, Science 342 (2013) 341–344.
[7] A. Yella, L.P. Heiniger, P. Gao, M.K. Nazeeruddin, M. Grätzel, Nano Lett. 14 (2014) 2591–2596.
[8] W. Chen, Y.Z. Wu, Y.F. Yue, J. Liu, W.J. Zhang, X.D. Yang, H. Chen, E.B. Bi, I. Ashraful, M. Grätzel4, L.Y. Han, Science 350 (2015) 944–948.
[9] X. Li, D.Q. Bi, C.Y. Yi, J.D. Décoppet, J.S. Luo, S.M. Zakeeruddin, A. Hagfeldt, M. Grätzel, Science 353 (2016) 58–62.
[10] S. De Wolf, J. Holovsky, S.J. Moon, P. Löper, B. Niesen, M. Ledinsky, F.J. Haug, J.H. Yum, C. Ballif, J. Phys. Chem. Lett. 5 (2014) 1035–1309.
[11] J.H. Noh, S.H. Im, J.H. Heo, T.N. Mandal, S.I. Seok, Nano Lett. 13 (2013) 1764–1769.
[12] Q. Wang, Y. Shao, Q. Dong, Z. Xiao, Y. Yuan, J. Huang, Energy Environ. Sci. 7 (2014) 2359–2365.
[13] A. Dualeh, N. Tétreault, T. Moehl, P. Gao, M.K. Nazeeruddin, M. Grätzel, Adv. Funct. Mater. 24 (2014) 3250–3258.
[14] M. Qian, M. Li, X. Shi, H. Ma, Z.K. Wang, L. Liao, J. Mater. Chem. 3 (2015) 13533–13539.
[15] D. Liu, T.L. Kelly, Nat. Photon. 8 (2014) 133.
[16] F. Zuo, S.T. Williams, P.W. Liang, C.C. Chueh, C.Y. Liao, A.K.Y. Jen, Adv. Mater. 26 (2014) 6454–6460.
[17] M.A. Green, A. Ho-Baillie, H.J. Snaith, Nat. Photon. 8 (2014) 506.
[18] Y.C. Shao, Z.G. Xiao, C. Bi, Y.B. Yuan, J.S. Huang, Nat. Commun. 5 (2014) 5784.
[19] T. He, Z. Liu, Y. Zhou, H. Ma, Solar energy mater. Sol. Cells 176 (2018) 280–287.
[20] G. Yang, H. Tao, P.L. Qin, W.J. Ke, G.J. Fang, J. Mater. Chem. 4 (2016) 3970–3990.
[21] A. Babayigit, A. Ethirajan, M. Muller, B. Conings, Nat. Mater. 15 (2016) 247.
[22] C.B. Fei, J.J. Tian, Y.J. Wang, X.G. Liu, L.L. Lv, Z.X. Zhao, G.Z. Cao, Nanomater. Energy 10 (2014) 353–365.
[23] D.Y. Son, J.H. Im, H.S. Kim, N.G. Park, J. Phys. Chem. C 118 (2014) 16567–16573.
[24] J. You, L. Meng, T.B. Song, T.F. Guo, Y.M. Yang, W.H. Chang, Z. Hong, H. Chen, H. Zhou, Q. Chen, Y. Liu, N. De Marco, Y. Yang, Nat. Nanotechnol. 11 (2015) 75.
[25] M. Singh, T.R. Rana, S. Kim, K. Kim, J.H. Yun, J. Kim, ACS Appl. Mater. Interfaces 8 (2016) 12764–12771.
[26] C. Liu, W. Li, C. Zhang, Y. Ma, J. Fan, Y. Mai, J. Am. Chem. Soc. 140 (2018) 3825–3828.
[27] J.L. Wu, W.K. Huang, Y.C. Chang, B.C. Tsai, Y.C. Hsiao, C.Y. Chang, C.T. Chen, J. Mater. Chem. 5 (2017) 12811–12821.
[28] M.M. Lee, J. Teuscher, T. Miyasaka, T.N. Murakami, H.J. Snaith, Science 338 (2012) 643–647.
[29] Z. Liu, T. He, K. Liu, J. Wang, Y. Zhou, J. Yang, H. Liu, Y. Jiang, H. Ma, M. Yuan, J. Mater. Chem. 5 (2017) 24282–24291.
[30] S. Seo, I.J. Park, M. Kim, S. Lee, C. Bae, H.S. Jung, N.G. Park, H. Shin, Nanoscale 8

(2016) 11403–11412.
[31] Z.K. Wang, M. Li, D.X. Yuan, X.B. Shi, H. Ma, L.S. Liao, ACS Appl. Mater. Interfaces 7 (2015) 9645–9651.
[32] Z. Liu, T. He, H. Wang, X. Song, H. Liu, J. Yang, K. Liu, H. Ma, RSC Adv. 7 (2017) 18456–18465.
[33] M. Saliba, T.K. Wee, S. Hiroaki, D.T. Moore, S. Trent, W. Zhang, L.A. Estroff, W. Ulrich, H.J. Snaith, J. Phys. Chem. C 118 (2014) 17171–17177.
[34] Z. Liu, T. He, K. Liu, Q. Zhi, M. Yuan, RSC Adv. 7 (2017) 26202–26210.
[35] S. Bai, Z.W. Wu, X.J. Wu, Y.Z. Jin, N. Zhao, Z.H. Chen, Q.Q. Mei, X. Wang, Z.Z. Ye, T. Song, Nano Res 12 (2014) 1749–1758.
[36] D.X. Yuan, A. Gorka, M.F. Xu, Z.K. Wang, L. Liao, Phys. Chem. Chem. Phys. 17 (2015) 19745–19750.
[37] M.F. Xu, L.S. Cui, X.Z. Zhu, C.H. Gao, X.B. Shi, Z.M. Jin, Z.K. Wang, L.S. Liao, Org. Electron. 14 (2013) 657–664.
[38] E. Mammadov, N. Naghavi, Z. Jehl, G. Renou, T. Tiwald, N. Mamedov, D. Lincot, J.F. Guillemoles, Thin Solid Films 571 (2014) 593–596.
[39] U. Palanchoke, H. Kurz, R. Noriega, S. Arabi, V. Jovanov, P. Magnus, H. Aftab, A. Salleo, H. Stiebig, D. Knipp, Nanomater. Energy 6 (2014) 167–172.
[40] A.K.K. Kyaw, D.H. Wang, D. Wynands, J. Zhang, T.Q. Nguyen, G.C. Bazan, A.J. Heeger, Nano Lett. 13 (2013) 3796–3801.
[41] W. Xu, J.A. McLeod, Y. Yang, Y. Wang, Z. Wu, S. Bai, Z. Yuan, T. Song, Y. Wang, J. Si, R. Wang, X. Gao, X. Zhang, L. Liu, B. Sun, ACS Appl. Mater. Interfaces 8 (2016) 23181–23189.
[42] W. Nie, H. Tsai, R. Asadpour, J.C. Blancon, A.J. Neukirch, G. Gupta, J.J. Crochet, M. Chhowalla, S. Tretiak, M.A. Alam, Science 347 (2015) 522–525.
[43] F. Huang, Y. Dkhissi, W. Huang, M. Xiao, I. Benesperi, S. Rubanov, Y. Zhu, X. Lin, L. Jiang, Y. Zhou, Nanomater. Energy 10 (2014) 10–18.
[44] M.J. Frisch, G.W. Trucks, H.B. Schlegel, G.E. Scuseria, M.A. Robb, J.R. Cheeseman, V.G. Zakrzewski, J.A. Montgomery Jr., R.E. Stratmann, J.C. Burant, S. Dapprich, J.M. Millam, A.D. Daniels, K.N. Kudin, M.C. Strain, O. Farkas, J. Tomasi, V. Barone, M. Cossi, R. Cammi, B. Mennucci, C. Pomelli, C. Adamo, S. Clifford, J. Ochterski, G.A. Petersson, P.Y. Ayala, Q. Cui, K. Morokuma, D.K. Malick, A.D. Rabuck, K. Raghavachari, J.B. Foresman, J. Cioslowski, J.V. Ortiz, B.B. Stefanov, G. Liu, A. Liashenko, P. Piskorz, I. Komaromi, R. Gomperts, R.L. Martin, D.J. Fox, T. Keith, M.A. Al-Laham, C.Y. Peng, A. Nanayakkara, C. Gonzalez, M. Challacombe, P.M.W. Gill, B. Johnson, W. Chen, M.W. Wong, J.L. Andres, C. Gonzalez, M. Head-Gordon, E.S. Replogle, J.A. Pople, Gaussian 03, Revision D.01, Gaussian, Inc., Pittsburgh PA, 2005.
[45] C.C. Zhang, M. Li, Z.K. Wang, Y.R. Jiang, H.R. Liu, Y.G. Yang, X.Y. Gao, H. Ma, J. Mater. Chem. 5 (2017) 2572–2579.
[46] J.M. Frost, K.T. Butler, F. Brivio, C.H. Hendon, M. Van Schilfgaarde, A. Walsh, Nano Lett. 14 (2014) 2584–2590.
[47] C. Li, Z. Zang, C. Han, Z. Hu, X. Tang, J. Du, Y. Lengb, K. Sun, Nanomater. Energy 40 (2017) 195–202.
[48] D. Wei, J. Ji, D. Song, M. Li, P. Cui, Y. Li, J.M. Mbengue, W. Zhou, Z. Ningc, N. Parkd, J. Mater. Chem. 5 (2017) 1406–1414.
[49] R. Zhang, C. Fei, B. Li, H. Fu, J. Tian, G. Cao, ACS Appl. Mater. Interfaces 9 (2017) 9785–9794.
[50] B. Lee, S. Chung, S.L. Kang, Acta Mater. 48 (2000) 1575–1580.
[51] W. Rheinheimer, M.J. Hoffmann, J. Mater. Sci. 51 (2016) 1756–1765.
[52] B. Conings, L. Baeten, C. De Dobbelaere, J. D'Haen, J. Manca, H.G. Boyen, Adv. Mater. 26 (2014) 2041–2046.
[53] X. Zhao, H. Shen, Y. Zhang, X. Li, X. Zhao, M. Tai, J. Li, J. Li, X. Li, H. Lin, ACS Appl. Mater. Interfaces 8 (2016) 7826–7833.
[54] Y. Cheng, Q.D. Yang, J. Xiao, Q. Xue, H.W. Li, Z. Guan, H.L. Yip, S.W. Tsang, ACS Appl. Mater. Interfaces 7 (2015) 19986–19993.
[55] C.H. DePuy, J.J. Grabowski, V.M. Bierbaum, S. Ingemann, N.M. Nibbering, J. Am. Chem. Soc. 107 (1985) 1093–1098.
[56] P. Docampo, J.M. Ball, M. Darwich, G.E. Eperon, H.J. Snaith, Nat. Commun. 4 (2014) 2761.
[57] Q. Chen, H.P. Zhou, Y.H. Fang, A.Z. Stieg, T.B. Song, H.H. Wang, X.B. Xu, Y.S. Liu, S.R. Lu, J.B. You, P.Y. Sun, J. Mckay, M.S. Goorsky, Y. Yang, Nat. Commun. 6 (2015) 7269.
[58] Z.G. Xiao, Q.F. Dong, C. Bi, Y.C. Shao, Y.B. Yuan, J.S. Huang, Adv. Mater. 26 (2014) 6503–6509.
[59] J.H. Heo, H.J. Han, D. Kim, T.K. Ahn, S.H. Im, Energy Environ. Sci. 8 (2015) 1602–1608.
[60] W.D. Callister, D.G. Rethwisch, John Wiley & Sons, Inc., NJ, USA, 2010, 665–721.
[61] A. Cho, S. Ahn, J.H. Yun, J. Gwak, H. Song, K. Yoon, J. Mater. Chem. 22 (2012) 17893–17899.
[62] Q. Wang, Y. Shao, H. Xie, L. Lyu, X. Liu, Y. Gao, J. Huang, Appl. Phys. Lett. 105 (2014) 163508.
[63] Q. Dong, Y. Fang, Y. Shao, P. Mulligan, J. Qiu, L. Cao, J. Huang, Science 347 (2015) 967–970.